First observations from the Kr multi-monochromatic x-ray imager for time and spatially resolved diagnosis of hot implosion cores

E. Gallardo-Diaz ✉ ⓘ ; R. C. Mancini ⓘ ; J. Clapp ⓘ ; P. Adrian ⓘ ; T. E. Evans ⓘ ; J. Frenje ⓘ ; R. Florido ⓘ ;
M. K. G. Kruse ⓘ ; T. Nagayama ⓘ

Check for updates

View Online

Export Citation

15 July 2024 12:55:18

First observations from the Kr multi-monochromatic x-ray imager for time and spatially resolved diagnosis of hot implosion cores

View Online   Export Citation   CrossMark

E. Gallardo-Diaz,[1,a)] R. C. Mancini,[1] J. Clapp,[1] P. Adrian,[2] T. E. Evans,[2] J. Frenje,[2] R. Florido,[3] M. K. G. Kruse,[4] and T. Nagayama[5]

AFFILIATIONS

[1] Physics Department, University of Nevada, Reno 89557, Nevada, USA

[2] Plasma Science Fusion Center, Massachusetts Institute of Technology, Cambridge 02139, Massachusetts, USA

[3] iUNAT-Departamento de Física, Universidad de Las Palmas de Gran Canaria, 35017 Las Palmas de Gran Canaria, Spain

[4] Lawrence Livermore National Laboratories, P.O. Box 808, Livermore 94550, California, USA

[5] Sandia National Laboratories, 1611 Innovation Pkwy SE, Albuquerque 87123, New Mexico, USA

Note: This paper is part of the Special Collection: Papers from the 65th Annual Meeting of the APS Division of Plasma Physics.
Note: Paper UI1 5, Bull. Am. Phys. Soc. **68** (2023).
a)Invited speaker. **Author to whom correspondence should be addressed:** enacgallardodiaz@gmail.com

ABSTRACT

This paper presents initial findings from the recently deployed Kr multi-monochromatic x-ray imager (Kr MMI) at the Omega laser facility. The experiment focuses on exploring implosion dynamics in exploding pusher capsules at three distinct initial gas fill densities. Utilizing time-gated and spatially integrated measurements, core size, electron temperature (T_e), and electron densities (n_e) are extracted through the analysis of the spectral region encompassing the Kr He α and its satellite lines. A comprehensive spectral database, incorporating atomic kinetics, spectroscopic-quality radiation transport, and Stark broadened line shapes, has been developed for rigorous data analysis. These measurements underscore the utility of the new Kr MMI instrument, which, combined with sophisticated analysis techniques, enables the diagnosis of plasma conditions at $T_e > 2000$ eV, thereby extending the capabilities beyond the prior Ar MMI design. This is an important stepping stone for achieving time-gated and space-resolved diagnostics of electron temperature, electron density, and heat transport in high temperature implosion cores.

I. INTRODUCTION

High-energy density physics is an interdisciplinary field dedicated to examining the behavior of matter in a plasma state, characterized by a broad spectrum of high temperatures and densities. A primary method for generating such extreme states involves direct drive inertial confinement fusion (ICF) experiments. In this approach, high-power laser beams are directed in a spherically symmetric configuration toward a millimeter-scale spherical capsule. This capsule, comprised of a shell and fuel containing fusion reactants, undergoes laser-induced ablation on its outer surface. Consequently, the inner shell functions as a piston, compelling the fuel to compress. This implosion results in an increase in the fuel density and temperature, creating a plasma state where the fusion reactions are held. ICF-type implosions are also employed as experimental platforms to perform basic high-energy density science to study, for example, ion stopping power,[1] electron–ion energy transfer,[2] and kinetic effects.[3] However, these implosion core plasmas exist within a highly confined region of both space (50–150 μm) and time (~0.5 ns) before the system undergoes expansion and cooling. Due to the plasma's extreme conditions, these systems prove challenging to diagnose and study. Essential parameters for understanding the ongoing processes within the plasma are its temperature and density. In this context, x-ray spectroscopy has emerged as a powerful technique to diagnose conditions within implosion cores.[4–18]

15 July 2024 12:55:18

X-ray spectroscopy serves as a valuable technique for diagnosing the electron temperature (T_e) and density (n_e) of plasma by leveraging the characteristic spectral signature of a spectroscopic tracer in the plasma. While solid dopants in the shell provide information on the conditions of the compressed shell plasma, gaseous tracers mixed in the capsule gas fill can be used to diagnose the core conditions. The emitted spectra of this tracer must exhibit sensitivity to T_e and n_e within the anticipated relevant ranges. Employing collisional radiative atomic kinetic models, detailed spectral line shapes, and spectroscopic-quality radiation transport, one can calculate the sensitivity of the spectra to the plasma conditions, enabling a comparison with the experimental data.

Historically, the use of argon K-shell (photon energy 3–4.5 keV) has been prevalent as a spectroscopic tracer for diagnosing core T_e and n_e.[18,19] However, the usefulness of the Ar K-shell spectrum diminishes significantly for T_e values exceeding 2000 eV due to the increasing ionization of electronic states responsible for these line transitions. To address the need for diagnosing these hot plasmas at T_e values surpassing 2000 eV, a higher Z spectroscopic tracer becomes imperative. Kr, as the higher Z noble gas succeeding Ar, emerges as an attractive alternative. Previous studies have demonstrated the utility of Kr K-shell (13–16 keV) in diagnosing hot implosion cores at the National Ignition Facility[20,21] and, more recently, at the Z machine in magnetized liner inertial fusion experiments.[22] Additionally, the Kr L-shell spectrum (2.7–3.5 keV) has exhibited sensitivity to T_e in the range of 1500–3000 eV.[23]

In this research, we add a tracer concentration of Kr to the gas fill and use the K-shell emission to diagnose T_e and n_e in hot ($T_e > 2000$ eV) implosion core experiments at the Omega laser facility. The shell of the capsules is made of Hoppe glass, and the gas fill contains a mixture of D_2, ^{3}He, and trace amounts of T and Kr. In order to detect the Kr K-shell line emission, we use two spectrometers: the x-ray spectrometer (XRS)[24] and a recently developed instrument known as the Kr multi-monochromatic x-ray imager (Kr MMI).[25]

This publication emphasizes spatially integrated measurements of the Kr MMI, specifically analyzing the core sizes from the He α spectral region and comparing the results with corresponding XRS measurements. In addition, we discuss the spectroscopic modeling employed and demonstrate our analysis method for extracting plasma conditions from spectroscopic data.

This paper is organized as follows: Sec. II describes the experimental setup used in these campaigns focusing on the Kr MMI instrument. Section III compares the core size measurements extracted from XRS and Kr MMI data. Next, Sec. IV discusses the model employed to develop the spectral database. Furthermore, this section shows the analysis method used to extract plasma conditions from the experimental measurements. Finally, Sec. V summarizes the conclusions of this research.

II. Kr MMI AND EXPERIMENTAL SETUP

The original design of the multi-monochromatic x-ray imager (MMI) was tailored to detect photon energy ranges corresponding to the Ar and Ti K-shell lines (3–6 keV). This version has found extensive application at the Omega laser facility, facilitating the diagnosis of both shell[26–32] and core conditions.[26,33–40] The need to utilize Kr K-shell lines for diagnosing plasma conditions in hot implosion cores prompted a modification of the instrument to capture the

corresponding photon energy range (12–16 keV). The design details of the Kr MMI are documented in a previous publication.[25]

The Kr MMI employs a pinhole array (PHA) to image the plasma, and these images are subsequently dispersed by a flat Ge (220) crystal into a time-gated micro-channel plate (MCP) detector. This diagnostic capability is particularly powerful, as it provides spectra with 2D (2-Dimensional) spatial resolution at four gated times. The characteristic feature of the MMI instrument is that it records gated arrays of spectrally resolved images. From these data, narrow- and broadband images as well as spatially integrated and resolved spectra can be extracted.[18,27] From this dataset, we can extract distributions of T_e and n_e in the core and observe their temporal evolution. These results offer valuable insight into implosion physics, including electron thermal transport and energy balance.

A refinement has been implemented in the Kr MMI design with respect to the one outlined in the preceding publication.[25] To improve the instrument performance, a specific adjustment has been made to the position of the PHA, denoted as Zpha in Ref. 25, shifting it from -1.2 to -1.29 mm. Additionally, the PHA height, represented by Hpha, has been reduced from 2.323 to 2.144 mm. These alterations ensure that all incident light entering the spectrometer undergoes reflection off the crystal. Furthermore, the inner radius of the cylindrical nose has been augmented to prevent any potential clipping on its inner surface.

As of November 2023, the Kr MMI has been fielded in three distinct Omega campaigns, producing successful and valuable data. The different experiments explored different regions in parameter space varying laser energy, gas fill pressure, and shell thickness. However, this paper will focus on the third campaign conducted in August 2023, as it was the first one to use four time-gated MCP measurements and the first one to collect He β data due to the high T_e achieved.

The experiment employs a 1 ns square laser pulse with a total energy output of 25 kJ distributed over 60 beams arranged in spherical symmetry. The 960 μm diameter capsule has a 6 μm thick shell made out of Hoppe glass. Variations in the gas fill pressure were introduced, with values set at 20, 11, and 7 atm. The gas mixture consisted of approximately 90% D_2, 10% ^{3}He, and trace amounts of T_2 and Kr, specifically at 0.01 atm each. To characterize the resulting plasma, a combination of x-ray and particle diagnostics was employed, with a particular emphasis on x-ray diagnostics as the focal point of this paper.

In these experiments, the XRS was fielded to compare with observations obtained with the Kr MMI system. The lines-of-sight were ($\theta = 37.28°$, $\phi = 162.0°$) for the XRS and ($\theta = 63.44°$, $\phi = 126.0°$) for the Kr MMI, where θ and ϕ represent the polar and azimuthal angular coordinates, respectively. The XRS is a flat crystal spectrometer capable of generating 1D (1-Dimensional) spatially resolved spectra when employed in conjunction with a slit. For detection in the Kr K-shell region, a Ge (111) crystal was utilized, along with a 25 μm slit and an image plate as detector. It is important to note a distinction from the Kr MMI: the XRS instrument operates on a temporally integrated basis. Consequently, the data generated by this instrument provide information on the temporally averaged conditions of the implosion, in contrast to the time-gated data obtained from the Kr MMI.

Figure 1 provides a visual representation of the spatial resolution difference between the two spectrometers. The XRS instrument's employment of a slit enables the resolution of one spatial dimension by integrating across a disk of thickness defined by the instrument's spatial
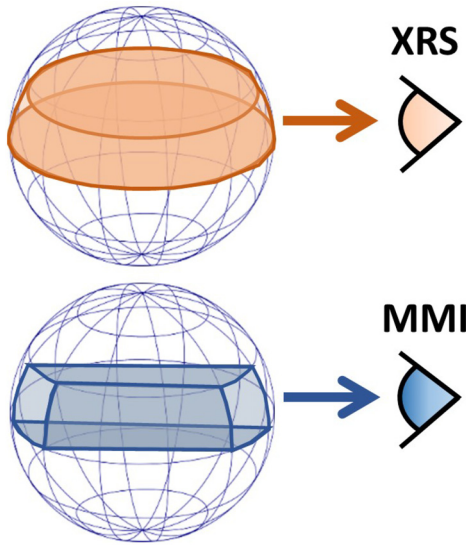
FIG. 1. Schematic representation illustrating the distinct volumes of integration for x-ray spectrometer (XRS) and multi-monochromatic imaging (MMI) in a spherical plasma. The XRS utilizes a slit, enabling the resolution of one spatial dimension by integrating over the emitted light within a disk limited by the instrument's spatial resolution. In contrast, MMI employs pinholes, allowing the resolution of two spatial dimensions by integrating over a chord of finite cross section, also constrained by the instrument's spatial resolution.

resolution. Conversely, the Kr MMI, utilizing pinholes, resolves two spatial dimensions by integrating along a chord with a finite cross section, restricted by the instrument's spatial resolution. To quantify the spatial resolution of the instruments including diffraction effects, we followed the methodology detailed in the Kr MMI design paper[25] and in Ref. 41. The estimated spatial resolution for the MMI, employing 13 μm diameter pinholes, is approximately 20.8 μm at 13 keV.

In Fig. 2, examples of data from both the XRS and MMI after correcting for their respective filter and detector responses are presented.
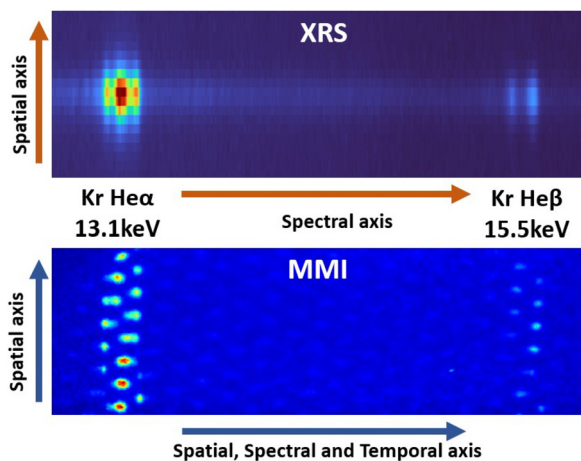
FIG. 2. XRS and MMI data after filter and detector response correction. Kr He α and He β emission regions are labeled.

The MMI data display one of the four time-gated frames, while the XRS data show time-integrated measurements. Both sets of images depict the emission regions of Kr He α and He β. While the vertical axis serves as a spatial reference in both cases, the horizontal axis takes on different roles. For XRS, it denotes the spectral axis. In contrast, for MMI, this axis encompasses spatial, spectral, and temporal dimensions. The temporal dimension arises from the pulse sweep of the MCP strip, moving from left to right across the image to detect the signal at different moments in time.

III. CORE SIZE ANALYSIS

The spatial resolution provided by both XRS and MMI enables the estimation of the core size, defined here as the size of the Kr K-shell line emission region. This diameter represents the spatial extent of the spherical core volume with sufficient temperature to ionize Kr and populate the upper energy levels of the n = 2 to n = 1 line transitions. The estimate of the core size of each measurement is used as input for the radiation transport modeling of the spectral database.

A forward reconstruction method utilizing the system's point spread function (PSF), as detailed in Ref. 41, is employed for this purpose. Equation (1) in this report outlines the image intensity profile on the detector plane, denoted as $I(r)$, as the convolution of the source profile $S(r)$ with the different PSFs of the system,

$$I(r) = S(r) * P_{geom}(r) * P_{diff}(r) * P_{bragg}(r) * P_{det}(r). \quad (1)$$

Figure 3 illustrates each PSF contributing to $I(r)$ in XRS. The geometric PSF is a rectangular function defined by the 25 μm slit aperture and instrument magnification. The detector, an image plate in this case, has a Gaussian PSF of 130 μm FWHM (full-width at half-maximum).[42] The Bragg PSF accounting for the effect of the Ge crystal is considered relatively minor leading to its neglect.[41] For diffraction contribution, the method and code from Ref. 41 are followed to calculate P_{diff} at 13 keV. In the near-field or Fresnel regime, as shown in Fig. 3, diffraction effects produce an oscillatory pattern, which, however, does not survive convolution with the remaining PSFs. $S(r)$ is
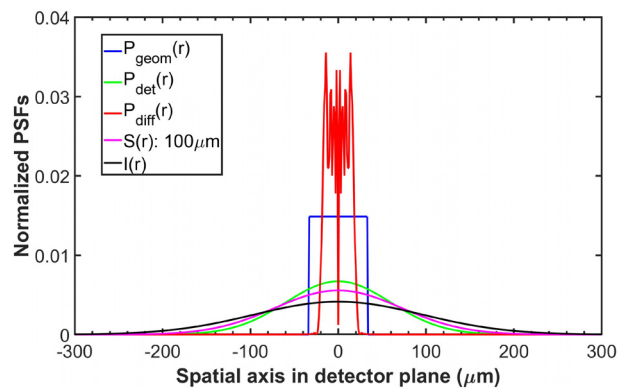
FIG. 3. Contributions to the final image intensity profile $I(r)$ formed in the detector plane for the case of XRS. $P_{geom}(r)$ represents the PSF of the 25 μm slit. $P_{diff}(r)$ is the PSF contribution due to diffraction effects at 13 keV. $P_{det}(r)$ is the image plate PSF. The $S(r)$ source profile is represented by a Gaussian function whose FWHM (full-width-half-maximum) is defined as the core size. In this case, we have used a core size of 100 μm to illustrate the convolution.

represented by a Gaussian function with a FWHM defining the core size.

The forward reconstruction algorithm employs an array of core sizes to generate a set of $I(r)$ profiles. This set is then compared to the XRS spatial lineouts of the Kr He α emission region using the Bayesian inference method similar to the one described in Sec. IV. This analysis enables the estimation of the core size along with its associated uncertainty.

For the Kr MMI, P_{geom} is defined by a 13 μm pinhole, and P_{det} is a 50 μm FWHM Gaussian function representing the MCP resolution.[41] Diffraction effects are considered by calculating P_{diff} for the Kr MMI system.

Figure 4 displays time-gated MMI (data points) and time-integrated XRS (broken lines) core size estimated using the forward reconstruction method for three different capsule fill pressures: 20, 11, and 7 atm. The solid line represents the linear fit to the MMI data points for each case. XRS measurements indicate a reduction in core size with decreasing initial pressure as detailed in Table I. This trend aligns with the expectation of higher core convergence due to lower gas pressure, as supported by 1-D hydrodynamic simulations performed with HYADES.[43] However, these simulations underpredict the core size at lower initial pressures.

MMI measurements enable the study of the time evolution of the core size between 1.2 and 1.52 ns relative to the leading edge of the laser pulse. The data illustrate the decreasing trend of core size with decreasing initial pressure. Additionally, the core size decreases with time for all cases except the 11 atm case, which shows a relatively constant diameter. The reduction in the size of the core region emitting the Kr He α line with time suggests either ongoing compression, cooling of the core, or a combination of both.

Comparing XRS and MMI core sizes reveals that time-gated measurements are consistently smaller than time-integrated ones. This suggests a period during the implosion, likely preceding the gated measurements at 1.2 ns, where the size of the region emitting the Kr line was larger than that measured during this specific time window.

IV. SPECTROSCOPIC ANALYSIS

In this section, we outline the modeling and analysis method applied to the Kr spectra. First, the plasma atomic kinetics are modeled
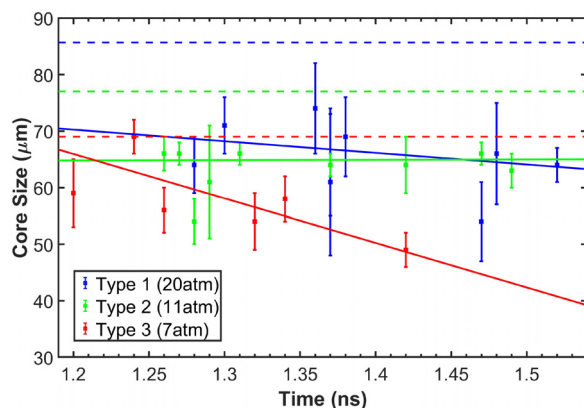
TABLE I. Core size diameters from XRS time-integrated measurements and HYADES hydrodynamic simulations.

Initial pressure (atm)	XRS (μm)	Hydro simulation (μm)
20	86 ± 4	84
11	77 ± 4	56
7	69 ± 4	40

across a range of T_e and n_e, considering a uniform sphere with a diameter corresponding to the average measured core size. This modeling yields the plasma level population. Next, the line shapes are calculated, incorporating Stark broadening effects and using the calculated level population. The modeled data are used to calculate the total emissivity and opacity distributions. Subsequently, the radiation transport equation is solved for each dataset's core size, assuming a uniform sphere, to determine the emergent intensity distribution (EID). It is worth noting that radiation transport is integrated into two stages of our model: within the atomic kinetic calculations utilizing the average measured core size and during the computation of the emergent intensity distribution, where the measured core size is customized for each dataset. Finally, leveraging the database of emergent intensity distributions, we employ a Bayesian inference method to fit the experimental spectrum. This approach yields the most probable values for T_e and n_e, along with their respective uncertainties.

PrismSpect[44] was employed for modeling the plasma collisional radiative atomic kinetics, producing level populations (N) for various combinations of T_e and n_e. These calculations were conducted using the Kr atomic model outlined in our previous study of the Kr L-shell region,[23] which is detailed in Table II of Ref. 45. The former reference demonstrates a notable agreement in the plasma charge state distribution (CSD) between PrismSpect and another collisional radiative atomic kinetics code (ABAKO)[45] calculation. The Kr L-shell publication[23] shows a detailed study of the CSD and its sensitivity with T_e and n_e, which is also applicable to this research. The simulations in the current paper maintained a non-LTE approach using a fine structure level of description, with radiation transport being solved in line with atomic kinetic equations tailored for a spherical plasma with a diameter of 62 μm, which is the average core size measured for this experimental campaign.

The multi-electron radiator line shape code (MERL)[46] used these populations as input for conducting detailed Stark broadening calculations of the line profiles (Φ). In these calculations, flexible atomic code[47] was utilized to obtain the atomic physics input needed for MERL, like the transition energy and transition rates (A). The methodology employed to calculate the line shapes of Kr He α and its satellites follows the approach outlined in a prior study concerning the Stark broadening effect on He β and its accompanying satellites.[48] MERL simulations employed the adjustable parameter exponential code[49] to compute the plasma microfield distribution at various n_e. Line profiles were calculated based on the standard Stark broadening theory approximation,[50] assuming static ions and dynamic electrons. Specifically, for Kr He α and its satellites, the line profiles considered encompassed the Kr He α resonance and intercombination line, along with Li-like n = 2, 3, and 4 satellites, and Be-like n = 2 satellites.

Since the amount of the Kr tracer is small and hence the majority of the perturbing ions in the plasma are lighter D and ^{3}He ions, it is

FIG. 4. MMI core size measurements (data points) and linear best fit trends (solid lines) for the three different initial pressures. XRS time-integrated core sizes are also represented (broken lines) and present an uncertainty of $\pm 4\,\mu$m.

important to check the effect of ion motion (i.e., ion dynamics) on the spectral line shapes. To this end, we also calculated the Kr He α line profile with an extended version of MERL that includes ion dynamics using the Boercker–Iglesias–Dufty model.[7] The results of these calculations are summarized in Table II in terms of the FWHM of the line profile. The values in Table II show the importance of ion dynamics in the Stark broadening of the Kr He α spectral line shape.

These calculations were performed for equal electron and ion temperatures $T_e = T_i = 3000$ eV, for which the Doppler FWHM is 3.62 eV. Also, included in Table II are the representative values of the optical depth of the He α transition for relevant implosion core sizes as well as the FWHM due to radiation transport broadening. While the FWHM values are useful to assess different broadening contributions, they do not capture all aspects of the detailed spectral line shapes included in this work, such as characteristic asymmetries and line wings, which are dominated by the Stark effect of static ions.

Next, the atomic level populations and the spectral line shapes are included in the calculation of the photon energy-resolved emissivity [$j(h\nu)$] and opacity [$k(h\nu)$] through the following equations:[23]

$$j(h\nu) = \sum_{\alpha\beta} \frac{h\nu}{4\pi} N_\beta A_{\beta\alpha} \Phi_{\alpha\beta}(h\nu), \quad (2)$$

$$k(h\nu) = \sum_{\alpha\beta} \frac{h\nu}{4\pi} (N_\alpha B_{\alpha\beta} - N_\beta B_{\beta\alpha}) \Phi_{\alpha\beta}(h\nu), \quad (3)$$

where α and β represent the lower and upper states of each transition, respectively. N_α is the population of α level, $\Phi_{\alpha\beta}(h\nu)$ is the line profile, and $A_{\alpha\beta}$ and $B_{\alpha\beta}$ are the Einstein coefficients of the transition from states α to β.

Figure 5 illustrates the total emissivity $j(h\nu)$ of Kr n = 2 to n = 1 line transitions and contribution breakdown computed from Eq. (2) for $T_e = 2000$ eV and $n_e = 10^{24}$/cc. This plot shows the complexity of this spectral region due to the overlap among the contributions of the different ions. Specifically, the Be- and Li-like contributions overlap in the region between 12.94 and 13.03 keV also containing the He α intercombination line (IC) at 13.026 keV. Furthermore, the He α resonance line overlaps with the Li-like n = 3 and n = 4 satellites. It is worth noting that the He α resonance line becomes optically thick (optical depth ≥ 1) for many of the n_e values considered in our model. Similarly, the IC line and the main Li-like peak at 13.05 keV become optically thick for high-density scenarios within our range of interest. For instance, at $T_e = 3000$ eV and $n_e = 5 \times 10^{23}$/cc the optical depth of He α resonance = 3.7; He α IC = 1.0; and Li-like main peak = 0.9. The high optical depth of these lines underscores the significance of accurately estimating the core size of each measurement.

TABLE II. Kr He α resonance line broadening effects. The data represent the FWHM of the line when different effects are applied: Static ions (SI), dynamic electrons (DE), ion dynamics (ID), and radiation transport (RT). The last column shows the optical depth (OD) of the line.

| n_e (/cc)	SI + DE (eV)	SI + DE + ID (eV)	SI + DE + ID + RT (eV)	OD
1×10^{24}	0.083	0.126	0.39	7.6
5×10^{24}	0.427	0.606	3.6	26
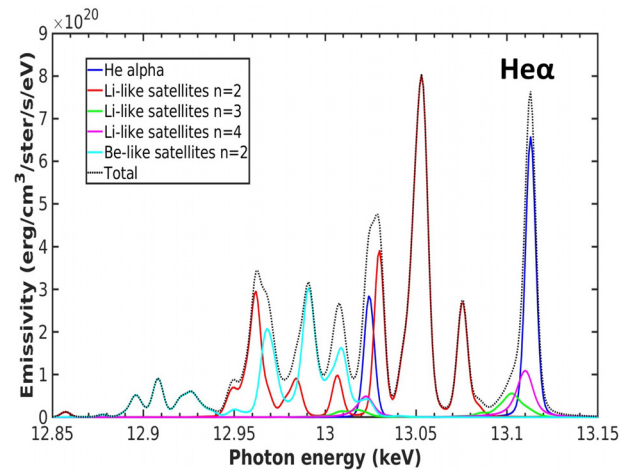
FIG. 5. Total emissivity of Kr n = 2 to n = 1 line transitions and contribution breakdown for $T_e = 2000$ eV and $n_e = 10^{24}$/cc.

Following the methodology outlined in a previous paper,[23] $j(h\nu)$ and $k(h\nu)$ were utilized to compute the emergent intensity distribution (EID) of a uniform sphere[51] using the diameter measured for each dataset. The resultant EID, generated for various combinations of T_e and n_e, formed a spectral database. Subsequently, convolution with a Gaussian function, characterized by a FWHM corresponding to the spectral resolution of each instrument, was performed. This facilitated the implementation of Bayesian analysis to estimate the plasma conditions.

Figures 6 and 7 depict the sensitivity of the EID with respect to T_e and n_e, respectively. In these figures, the EID is convolved with a 21.9 eV FWHM Gaussian, representing the MMI spectral resolution. All traces are normalized to the He α resonance line for comparative analysis.
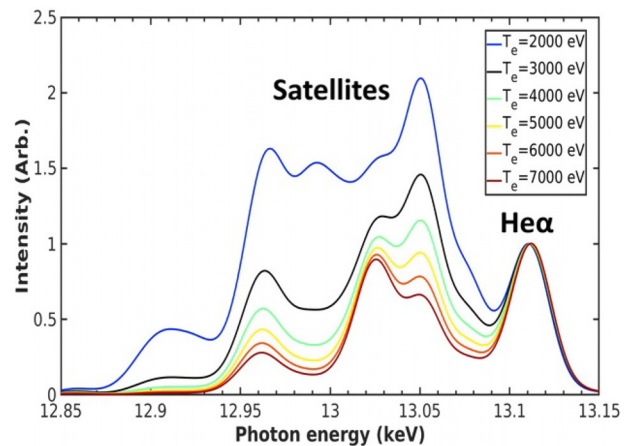
FIG. 6. Kr He α emergent intensity distribution T_e sensitivity at $n_e = 10^{24}$/cc. The spectra contain contributions from the spectral lines labeled in Fig. 5. This case corresponds to a 62 μm diameter core and convolved with a 21.9 eV Gaussian function to account for the MMI spectral resolution. The black trace corresponds to the black trace also shown in Fig. 7 at $T_e = 3$ keV and $n_e = 10^{24}$/cc.
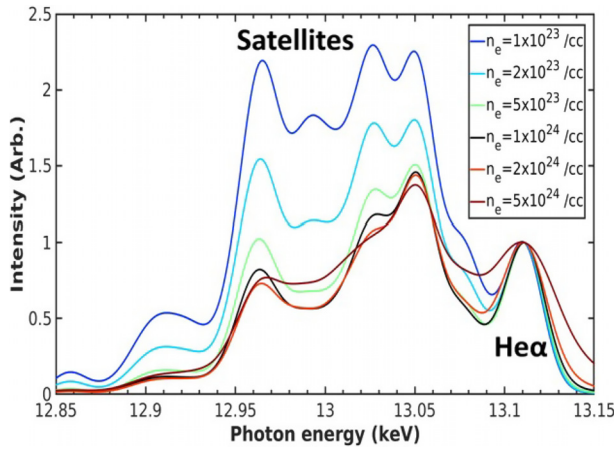
FIG. 7. Kr He α emergent intensity distribution n_e sensitivity at $T_e = 3000$ eV. The spectra contains contributions from the spectral lines labeled in Fig. 5. This case corresponds to a 62 μm diameter core and convolved with a 21.9 eV Gaussian function to account for the MMI spectral resolution. The black trace corresponds to the black trace also shown in Fig. 6 at $T_e = 3$ keV and $n_e = 10^{24}$/cc.

FIG. 8. Corner plot displaying the posterior probability distribution function for the spatially integrated data from frame number 2 of shot s109 486 in the MMI dataset (P = 20 atm, t = 1.37 ns, diameter = 61 μm). The color map represents the posterior probability distribution in parameter space, with red representing the maximum value. The top and right plots present the marginalized distributions for n_e and T_e, respectively. The dashed vertical line indicates the expected value. The titles of both plots specify the estimated values of n_e and T_e, along with their uncertainties derived from the FWHM of the distributions.

In Fig. 6, the ionization of lower charged states producing the satellite lines is evident with increasing T_e. Additionally, the central double peak structure shape changes with T_e due to the increase in the relative emission of the He α IC line with respect to the satellite lines. These effects result in spectra that are sensitive to T_e within the 1500–7000 eV range.

Figure 7 illustrates the sensitivity of the line profiles with n_e. The change in the spectra is a result of the dependence of the atomic kinetics and the Stark broadening effect with n_e. Particularly, the impact of Stark broadening is prominently observed in the fill of the valley between the He α resonance line and the primary Li-like satellite line at $n_e \geq 2 \times 10^{24}$.

To infer the plasma conditions from the recorded spectrum, we perform Bayesian analysis[52] using Bayes theorem for the case of our system. If $(y_1, y_2 \ldots)$ are the individual recorded intensities for each of the N data points that form the spectrum, then the posterior probability distribution [the probability that (T_e, n_e) generated spectrum $(y_1, y_2 \ldots)$] is
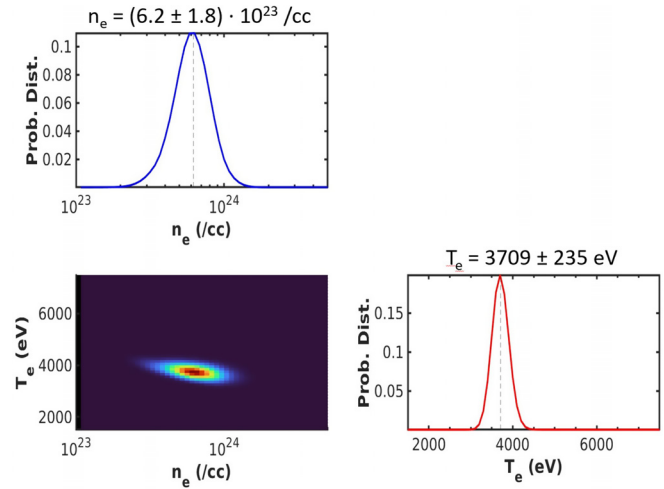
$$P(T_e, n_e | y_1, y_2, \ldots) = \frac{P(y_1, y_2 \ldots | T_e, n_e) P(T_e, n_e)}{P(y_1, y_2, \ldots)}, \quad (4)$$

where $P(T_e, n_e)$ corresponds to the prior probability distribution while $P(y_1, y_2, \ldots)$ is the evidence or normalization factor of the posterior. This normalization factor is chosen such that the integral over the total probability distribution is equal to one. The likelihood function $P(y_1, y_2, \ldots | T_e, n_e)$ is defined as follows:

$$P(y_1, y_2, \ldots | T_e, n_e) \equiv \prod_i^N \exp\left\{ -\frac{\left(y_i^{model}(T_e, n_e) - y_i\right)^2}{2\sigma_i^2} \right\}. \quad (5)$$

Here, σ_i represent the statistical weights associated with the error of the measurement and $y_i^{model}(T_e, n_e)$ are the intensities calculated in the spectral database for the different combinations of T_e and n_e.

We assume uniform prior probability distribution $P(T_e, n_e)$ = const within the region of interest in parameter space

$(T_e = 1500 - 7500$ eV and $n_e = 10^{23} - 5 \times 10^{24}/cc)$, which is appropriate when the likelihood function is non-zero only over finite parameter space. The sampling of the likelihood function is typically done using the Markov Chain Monte Carlo (MCMC) technique; however, in our case of application, this technique is not necessary since we only count with two parameters (i.e., T_e and n_e). Thus, we can numerically evaluate the likelihood function exhaustively as a function of T_e and n_e values.

Figure 8 illustrates the posterior distribution function for the MMI data in frame 2 from shot s109 486. This shot corresponds to a type 1 shot with 20 atm initial pressure timed at 1.37 ns and a measured core size of 61 μm. The expected values of the T_e and n_e probability distribution functions represent the most probable conditions given our experimental data. Furthermore, the FWHM of the distribution corresponds to the uncertainty of this measurement.

Figure 9 displays the experimental data alongside the best fit and fits within the uncertainty limits obtained through the Bayesian analysis. The fit effectively captures the overall spectral shape for both the He α line and its satellites. However, it does not accurately reproduce the relative intensity of the central double peak structure. From the analysis of these data, the extracted plasma conditions are $T_e = 3709$ eV and $n_e = 6.2 \times 10^{23}/cc$ with uncertainties of 6% and 29%, respectively. In addition to these uncertainties obtained from the fit of the data, we include an estimated 10% uncertainty arising from the choice of the spectral background subtraction region. Adding these contributions in quadrature, we obtain 12% and 31% uncertainty in the T_e and n_e, respectively.

Future investigations will explore a comprehensive analysis of the results obtained through this technique, focusing on both the time-integrated spectra from XRS and the time-gated MMI spatially integrated measurements. Furthermore, forthcoming work will include
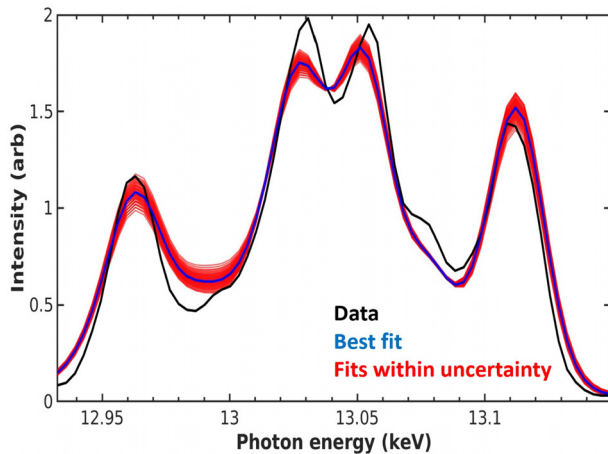
FIG. 9. Experimental spatially integrated spectrum (black) and best fit (blue) for MMI frame 2 data from s109 486. The best fit corresponds to the theoretical spectrum with $T_e = 3709$ eV and $n_e = 6.2 \times 10^{23}$/cc as shown in Fig. 8. Fits falling within the uncertainty limits are represented in red.

detailed data analysis of the MMI spatially resolved He β spectra, enabling the extraction of 2D maps depicting the spatial distribution of T_e and n_e. These findings will be presented in a subsequent publication.

V. CONCLUSIONS

This research marks a significant milestone with the introduction of the Kr MMI instrument at the Omega laser facility. The findings demonstrate the instrument's capability to yield electron temperature and density measurements in hot implosion cores ($T_e > 2000$ eV), a capability not attainable with the previous MMI version utilizing Ar as a spectroscopic tracer. The focus of this paper centers on the core size analysis of XRS and MMI as well as the development of a spectroscopic model and analysis method to diagnose plasma conditions. To this end, we present the Bayesian analysis conducted on one of the time-gated spatially integrated MMI datasets. A subsequent publication will explore the time-resolved, spatially integrated He α results and spatially resolved diagnostics analyzing the He β spectral region.

The analysis of MMI data has provided insight into the size of the Kr emission region, offering a comparative perspective with XRS time-integrated data. Time-gated measurements reveal a reduction in core size between 1.2 and 1.52 ns relative to the leading edge of the laser pulse. Contrastingly, time-integrated data indicate a larger core size than the time-gated MMI data, hinting at a larger size at earlier times. Both datasets reveal a decrease in core size with decreasing fill pressure, aligning with simulation expectations. However, simulations predict smaller core sizes at low fill pressures. The results of the core size measurements are included in the modeled spectral database used to analyze each dataset.

The development of a detailed emergent intensity distribution (EID) database has facilitated precise diagnosis of plasma conditions from Kr spectra. The combination of different modeling codes results in an EID that exhibits sensitivity with T_e and n_e. Employing Bayesian analysis, we obtain probability distributions for the plasma conditions, allowing for estimation of their most probable values and uncertainties. The best fit shows an overall good quality agreement with the experimental spectrum.

The new Kr MMI instrument emerges as a robust diagnostic tool that extends the capabilities of the previous Ar MMI, unlocking a new region in parameter space for time-gated and 2D spatially resolved spectroscopic measurements. The collected data hold the potential to offer valuable insight into implosion dynamics and plasma distributions. The time and spatial resolution offered by this instrument provide a distinct advantage over other spectrometers that lack the ability to resolve all these dimensions, such as XRS. Currently, we are in the process of designing two additional MMI configurations to target different spectral regions of interest: the Cu K-shell (7.5–10 keV) and the Ge K-shell (9–12.5 keV) MMIs. These new designs will expand the range of tracers usable with this instrument, thereby enhancing its versatility.

AUTHOR DECLARATIONS
Conflict of Interest

The authors have no conflicts to disclose.

Author Contributions

E. Gallardo-Diaz: Formal analysis (lead); Investigation (lead); Writing – original draft (lead); Writing – review & editing (lead). **R. C. Mancini:** Formal analysis (equal); Investigation (equal); Methodology (equal); Writing – review & editing (equal). **J. Clapp:** Formal analysis (supporting). **P. Adrian:** Investigation (supporting). **T. E. Evans:** Formal analysis (supporting); Investigation (equal); Writing – review & editing (supporting). **J. Frenje:** Funding acquisition (lead). **R. Florido:** Investigation (supporting). **M. K. G. Kruse:** Resources (equal). **T. Nagayama:** Investigation (supporting); Resources (supporting).

DATA AVAILABILITY

The data that support the findings of this study are available from the corresponding author upon reasonable request.

REFERENCES

[1]J. A. Frenje, R. Florido, R. Mancini, T. Nagayama, P. E. Grabowski, H. Rinderknecht, H. Sio, A. Zylstra, M. Gatu Johnson, C. K. Li *et al.*, Phys. Rev. Lett. **122**, 015002 (2019a).

[2]P. J. Adrian, R. Florido, P. E. Grabowski, R. Mancini, B. Bachmann, L. X. Benedict, M. G. Johnson, N. Kabadi, B. Lahmann, C. K. Li *et al.*, Phys. Rev. E **106**, L053201 (2022).

[3]M. J. Rosenberg, H. G. Rinderknecht, N. M. Hoffman, P. A. Amendt, S. Atzeni, A. B. Zylstra, C. K. Li, F. H. Séguin, H. Sio, M. G. Johnson *et al.*, Phys. Rev. Lett. **112**, 185001 (2014).

[4]C. F. Hooper, Jr., D. P. Kilcrease, R. C. Mancini, L. A. Woltz, D. K. Bradley, P. A. Jaanimagi, and M. C. Richardson, Phys. Rev. Lett. **63**, 267–270 (1989).

[5]R. C. Mancini, J. Hooper, C. F, N. D. Delamater, A. Hauer, C. J. Keane, B. A. Hammel, and J. K. Nash, Rev. Sci. Instrum. **63**, 5119–5121 (1992).

[6]C. J. Keane, B. A. Hammel, D. R. Kania, J. D. Kilkenny, R. W. Lee, A. L. Osterheld, L. J. Suter, R. C. Mancini, J. Hooper, C. F, and N. D. Delamater, Phys. Fluids B: Plasma Phys. **5**, 3328–3336 (1993).

[7]D. A. Haynes, D. T. Garber, C. F. Hooper, R. C. Mancini, Y. T. Lee, D. K. Bradley, J. Delettrez, R. Epstein, and P. A. Jaanimagi, Phys. Rev. E **53**, 1042–1050 (1996).

[8]R. Florido, R. C. Mancini, T. Nagayama, R. Tommasini, J. A. Delettrez, S. P. Regan, and B. Yaakobi, Rev. Sci. Instrum. **81**, 10E307 (2010a).

[9]R. Florido, R. Mancini, T. Nagayama, R. Tommasini, J. Delettrez, S. Regan, V. Smalyuk, R. Rodríguez, and J. Gil, High Energy Density Phys. **6**, 70–75 (2010b).

[10]R. Florido, R. C. Mancini, T. Nagayama, R. Tommasini, J. A. Delettrez, S. P. Regan, and B. Yaakobi, Phys. Rev. E **83**, 066408 (2011).

[11]R. Florido, R. C. Mancini, T. Nagayama, R. Tommasini, J. A. Delettrez, and S. P. Regan, Phys. Plasmas **21**, 102709 (2014).

[12]R. Florido and R. C. Mancini, J. Phys. B: At., Mol. Opt. Phys. **48**, 224006 (2015).

[13]S. P. Regan, J. A. Delettrez, R. Epstein, P. A. Jaanimagi, B. Yaakobi, V. A. Smalyuk, F. J. Marshall, D. D. Meyerhofer, W. Seka, D. A. Haynes *et al.*, Phys. Plasmas **9**, 1357–1365 (2002).

[14]I. Golovkin, R. Mancini, S. Louis, Y. Ochi, K. Fujita, H. Nishimura, H. Shirga, N. Miyanaga, H. Azechi, R. Butzbach *et al.*, Phys. Rev. Lett. **88**, 045002 (2002).

[15]T. Ma, H. Chen, P. K. Patel, M. B. Schneider, M. A. Barrios, D. T. Casey, H.-K. Chung, B. A. Hammel, L. F. Berzak Hopkins, L. C. Jarrott *et al.*, Rev. Sci. Instrum. **87**, 11E327 (2016).

[16]H. Chen, T. Ma, R. Nora, M. A. Barrios, H. A. Scott, M. B. Schneider, L. Berzak Hopkins, D. T. Casey, B. A. Hammel, L. C. Jarrott *et al.*, Phys. Plasmas **24**, 072715 (2017).

[17]M. J. May, G. E. Kemp, J. D. Colvin, D. A. Liedahl, P. L. Poole, D. B. Thorn, K. Widmann, R. Benjamin, M. A. Barrios, and B. E. Blue, Phys. Plasmas **26**, 063105 (2019).

[18]T. Nagayama, R. C. Mancini, R. Florido, D. Mayes, R. Tommasini, J. A. Koch, J. A. Delettrez, S. P. Regan, and V. A. Smalyuk, Phys. Plasmas **21**, 050702 (2014).

[19]M. Bailly-Grandvaux, R. Florido, C. A. Walsh, G. Pérez-Callejo, F. N. Beg, P. Bradford, M. A. Gigosos, R. C. Mancini, C. McGuffey, F. Suzuki-Vidal *et al.*, Phys. Rev. Res. **6**, L012018 (2024).

[20]L. Gao, B. F. Kraus, K. W. Hill, M. B. Schneider, A. Christopherson, B. Bachmann, M. Bitter, P. Efthimion, N. Pablant, R. Betti *et al.*, Phys. Rev. Lett. **128**, 185002 (2022).

[21]K. W. Hill, L. Gao, B. F. Kraus, M. Bitter, P. C. Efthimion, N. Pablant, M. B. Schneider, D. B. Thorn, H. Chen, R. L. Kauffman *et al.*, Plasma Phys. Controlled Fusion **64**, 105025 (2022).

[22]J. T. Clapp, R. C. Mancini, E. C. Harding, M. A. Schaeuble, and A. J. Harvey-Thompson, Rev. Sci. Instrum. **93**, 103532 (2022).

[23]E. Gallardo-Diaz, R. C. Mancini, K. R. Carpenter, P. Adrian, J. Frenje, and R. Florido, Phys. Plasmas **31**, 033302 (2024a).

[24]D. B. Thorn, F. Coppari, T. Döppner, M. J. MacDonald, S. P. Regan, and M. B. Schneider, Rev. Sci. Instrum. **89**, 10F119 (2018).

[25]E. Gallardo-Diaz, R. C. Mancini, D. T. Cliche, and R. Tommasini, Rev. Sci. Instrum. **93**, 113525 (2022).

[26]N. Izumi, T. W. Barbee, J. A. Koch, R. C. Mancini, and L. A. Welser, Rev. Sci. Instrum. **77**, 083504 (2006).

[27]R. C. Mancini, H. M. Johns, T. Joshi, D. Mayes, T. Nagayama, S. C. Hsu, J. A. Baumgaertel, J. Cobble, N. S. Krasheninnikova, P. A. Bradley *et al.*, Phys. Plasmas **21**, 122704 (2014).

[28]J. A. Baumgaertel, P. A. Bradley, S. C. Hsu, J. A. Cobble, P. Hakel, I. L. Tregillis, N. S. Krasheninnikova, T. J. Murphy, M. J. Schmitt, R. C. Shah *et al.*, Phys. Plasmas **21**, 052706 (2014).

[29]R. C. Shah, B. M. Haines, F. J. Wysocki, J. F. Benage, J. A. Fooks, V. Glebov, P. Hakel, M. Hoppe, I. V. Igumenshchev, G. Kagan *et al.*, Phys. Rev. Lett. **118**, 135001 (2017).

[30]B. Yaakobi, F. J. Marshall, and D. K. Bradley, Appl. Opt. **37**, 8074–8080 (1998).

[31]H. M. Johns, R. C. Mancini, P. Hakel, T. Nagayama, V. A. Smalyuk, S. P. Regan, and J. Delettrez, Phys. Plasmas **21**, 082711 (2014).

[32]H. M. Johns, R. C. Mancini, T. Nagayama, D. C. Mayes, R. Tommasini, V. A. Smalyuk, S. P. Regan, and J. A. Delettrez, Phys. Plasmas **23**, 012709 (2016).

[33]L. A. Welser, R. C. Mancini, J. A. Koch, S. Dalhed, R. W. Lee, I. E. Golovkin, F. Marshall, J. Delettrez, and L. Klein, Rev. Sci. Instrum. **74**, 1951–1953 (2003).

[34]R. Tommasini, J. A. Koch, N. Izumi, L. A. Welser, R. C. Mancini, J. Delettrez, S. Regan, and V. Smalyuk, Rev. Sci. Instrum. **77**, 10E303 (2006).

[35]D. T. Cliche and R. C. Mancini, Appl. Opt. **58**, 4753–4761 (2019).

[36]J. A. Koch, J. Barbee, T. W, N. Izumi, R. Tommasini, R. C. Mancini, L. A. Welser, and F. J. Marshall, Rev. Sci. Instrum. **76**, 073708 (2005).

[37]S. Laffite, J. L. Bourgade, T. Caillaud, J. A. Delettrez, J. A. Frenje, F. Girard, V. Y. Glebov, T. Joshi, O. Landoas, G. Legay *et al.*, Phys. Plasmas **23**, 012706 (2016).

[38]T. R. Joshi, P. Hakel, S. C. Hsu, E. L. Vold, M. J. Schmitt, N. M. Hoffman, R. M. Rauenzahn, G. Kagan, X.-Z. Tang, R. C. Mancini *et al.*, Phys. Plasmas **24**, 056305 (2017).

[39]T. R. Joshi, S. C. Hsu, P. Hakel, N. M. Hoffman, H. Sio, and R. C. Mancini, Phys. Plasmas **26**, 062702 (2019).

[40]S. C. Hsu, T. R. Joshi, P. Hakel, E. L. Vold, M. J. Schmitt, N. M. Hoffman, R. M. Rauenzahn, G. Kagan, X.-Z. Tang, R. C. Mancini *et al.*, Europhys. Lett. **115**, 65001 (2016).

[41]I. L. Tregillis, "Estimating the photonics budget, resolution, and signal requirements for a multi-monochromatic X-ray imager," Report No. LA-UR-16-27264 (Los Alamos National Lab.(LANL), Los Alamos, NM, 2016).

[42]J. F. Seely, G. E. Holland, L. T. Hudson, and A. Henins, Appl. Opt. **47**, 5753–5761 (2008).

[43]J. T. Larsen and S. M. Lane, J. Quant. Spectrosc. Radiat. Transfer **51**, 179–186 (1994).

[44]J. MacFarlane, I. Golovkin, P. Woodruff, D. Welch, B. Oliver, T. Mehlhorn, and R. Campbell, in *Proceedings of Inertial Fusion and Sciences Applications* (Sandia National Laboratory, 2003), Vol. 457.

[45]R. Florido, R. Rodríguez, J. M. Gil, J. G. Rubiano, P. Martel, E. Mínguez, and R. C. Mancini, Phys. Rev. E **80**, 056402 (2009).

[46]R. Mancini, D. Kilcrease, L. Woltz, and C. Hooper, Comput. Phys. Commun. **63**, 314–322 (1991).

[47]M. F. Gu, Can. J. Phys. **86**, 675–689 (2008).

[48]E. Gallardo-Diaz, R. C. Mancini, J. T. Clapp, and M. Kruse, "Krypton Heβ line spectrum including n = 2, 3 Li-like satellites with detailed Stark broadened line shapes," High Energy Density Phys. (published online, 2024b).

[49]C. Iglesias, F. Rogers, R. Shepherd, A. Bar-Shalom, M. Murillo, D. Kilcrease, A. Calisti, and R. Lee, J. Quant. Spectrosc. Radiat. Transfer **65**, 303–315 (2000).

[50]H. R. Griem, *Principles of Plasma Spectroscopy*, Cambridge Monographs on Plasma Physics (Cambridge University Press, 1997).

[51]T. Burris-Mog, R. Mancini, J. Bailey, G. Chandler, G. Rochau, G. Dunham, P. Lake, K. Peterson, S. Slutz, T. Mehlhorn *et al.*, J. Quant. Spectrosc. Radiat. Transfer **99**, 120–130 (2006).

[52]P. F. Knapp and W. E. Lewis, Rev. Sci. Instrum. **94**, 061103 (2023).